

# Vortex beam generation by spin-orbit coupling in Bloch surface waves

Ugo Stella<sup>1</sup>, Thierry Grosjean<sup>2</sup>, Natascia De Leo<sup>3</sup>, Luca Boarino<sup>3</sup>, Peter Munzert<sup>4</sup>, Joseph R. Lakowicz<sup>5</sup> and Emiliano Descrovi<sup>1\*</sup>

<sup>1</sup> Department of Applied Science and Technology (DISAT), Politecnico di Torino, Corso Duca degli Abruzzi 24, Torino, IT-10129, Italy.

<sup>2</sup> FEMTO-ST Institute, Université Bourgogne Franche-Comté, UMR CNRS 6174 15B Avenue des Montboucons, 25030, Besançon, France

<sup>3</sup> Quantum Research Labs & Nanofacility Piemonte, Nanoscience & Materials Division, Istituto Nazionale di Ricerca Metrologica (INRiM), Strada delle Cacce 91, Torino, IT-10135, Italy.

<sup>4</sup> Fraunhofer Institute for Applied Optics and Precision Engineering IOF, Albert-Einstein-Str. 7, Jena DE-07745, Germany

<sup>5</sup> Center for Fluorescence Spectroscopy, Department of Biochemistry and Molecular Biology, University of Maryland School of Medicine, Baltimore, Maryland 21201, United States

Mr. Ugo Stella: [ugo.stella@polito.it](mailto:ugo.stella@polito.it)

Dr. Thierry Grosjean: [thierry.grosjean@univ-fcomte.fr](mailto:thierry.grosjean@univ-fcomte.fr)

Dr. Natascia De Leo: [n.deleo@inrim.it](mailto:n.deleo@inrim.it)

Dr. Luca Boarino: [l.boarino@inrim.it](mailto:l.boarino@inrim.it)

Dr. Peter Munzert: [peter.munzert@iof.fraunhofer.de](mailto:peter.munzert@iof.fraunhofer.de)

Prof. Joseph R. Lakowicz: [JLakowicz@som.umaryland.edu](mailto:JLakowicz@som.umaryland.edu)

Corresponding Author:

Prof. Emiliano Descrovi: [emiliano.descrovi@polito.it](mailto:emiliano.descrovi@polito.it)

Phone: +39 011 090 7352

Fax: +39 011 090 7399

**Keywords:** Chiral nanostructures, Bloch Surface Waves, vortex beam

32 **ABSTRACT**

33 Axis-symmetric grooves milled in metallic slabs have been demonstrated to promote the transfer of  
34 Orbital Angular Momentum (OAM) from far- to near-field and vice versa, thanks to spin-orbit  
35 coupling effects involving Surface Plasmons (SP). However, the high absorption losses and the  
36 polarization constraints, which are intrinsic in plasmonic structures, limit their effectiveness for  
37 applications in the visible spectrum, particularly if emitters located in close proximity to the metallic  
38 surface are concerned. Here, an alternative mechanism for vortex beam generation is presented,  
39 wherein a free-space radiation possessing OAM is obtained by diffraction of Bloch Surface Waves  
40 (BSWs) on a dielectric multilayer. A circularly-polarized laser beam is tightly focused on the  
41 multilayer backside by means of an immersion optics, such that TE-polarized BSWs are launched  
42 radially from the focused spot. While propagating on the multilayer surface, BSWs exhibit a spiral-  
43 like wavefront due to the polarization-selective coupling mechanism. A spiral grating surrounding  
44 the illumination area provides for the BSW diffraction out-of-plane, by imparting an additional  
45 azimuthal geometric phase distribution defined by the topological charge of the spiral structure. At  
46 infinity, the constructive interference results into free-space beams with defined combinations of  
47 polarization and OAM satisfying the conservation of the Total Angular Momentum, based on the  
48 incident polarization handedness and the spiral grating topological charge. As an extension of this  
49 concept, chiral diffractive structures for BSWs can be used in combination with surface cavities  
50 hosting light sources therein.

51

52

53

54

55

56

57

58

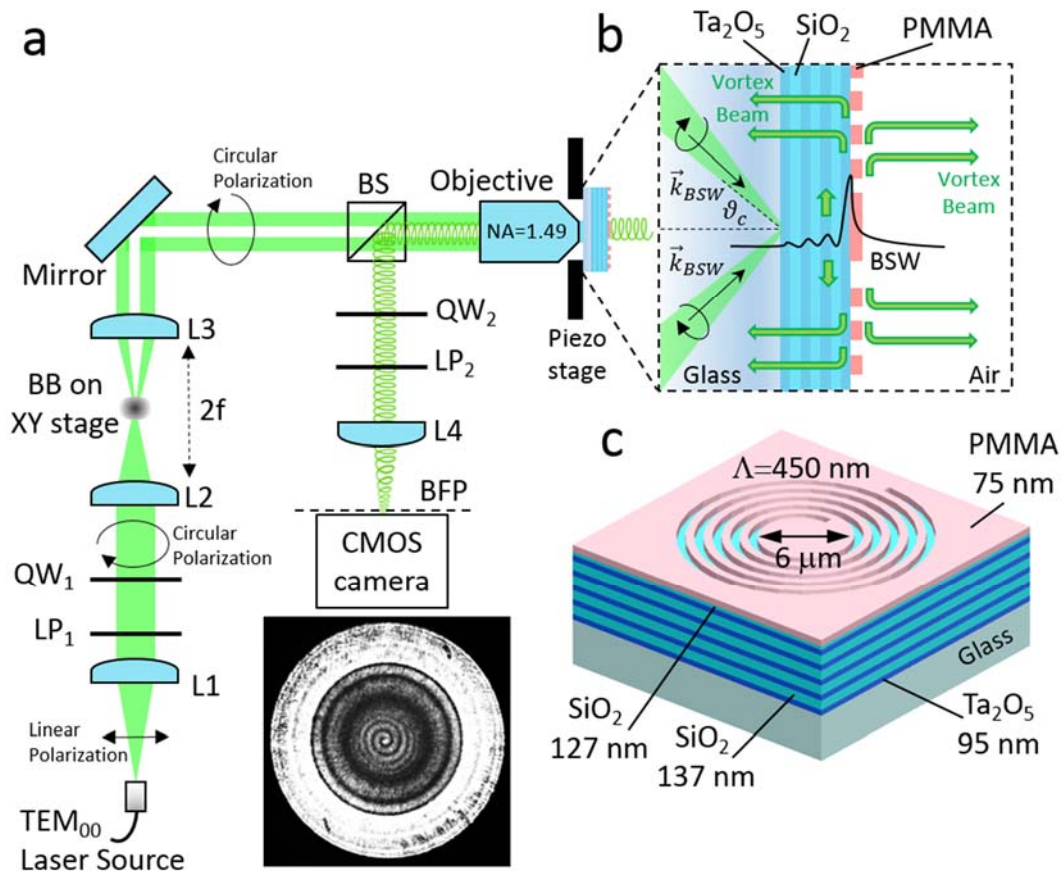
## 59 INTRODUCTION

60 Vortex beams represent a family of structured beams generally characterized by a phase singularity  
61 along the optical axis, a doughnut intensity distribution and an azimuthally-varying phase over a beam  
62 transverse cross-section [1,2]. When the polarization state is spatially inhomogeneous, the term  
63 Vectorial Vortex Beams is often used [3]. From a quantum-optics perspective, each vortex beam  
64 photon is provided with a quantized Orbital Angular Momentum (OAM) equal to  $\hbar\ell$ , where  $\ell$  is an  
65 integer indicating the topological charge of the vortex. In recent years, Vortex beams have gained an  
66 increasing popularity because of several new applications into different domains such as micro-  
67 particle manipulation and trapping [4-6], compact laser sources [7,8], microscopy [9,10] and optical  
68 communications [11,12]. Conventional methods for producing vortex beams [13] involve the use of  
69 (possibly tunable) anisotropic media such as Liquid Crystal [14,15] and q-plates [16] or hierarchically  
70 structured holograms encoding proper phase functions [17-20]. More recently, metasurfaces, which  
71 can be either dielectric or plasmonic, have been introduced in order to gather more degrees of freedom  
72 in OAM manipulation [21,22], through the control of so-called spin-orbit coupling effects mediated  
73 by the metasurface topology [23]. Metasurfaces are mainly employed as free-space beam converters,  
74 which have found applications also within laser cavities [24]. The concept of beam conversion  
75 through metasurfaces relies on a spatially-dependent phase manipulation of the scattered field. The  
76 output vortex beams result from a coherent sum of the scattered radiation originating from different  
77 portions of the surface, which is illuminated as a whole. However, this approach can be hardly  
78 adopted when the input field has a limited spatial extension (as for focused beams or localized  
79 coherent sources such as optical antennas or cavities), unless some mode coupling is intervening [25].  
80 This is indeed the case in structured metallic films, wherein the generation of free-space vortex beam  
81 carrying OAM occurs upon spin-orbit coupling and scattering/diffraction of plasmonic modes by  
82 means of nano-slits [26-28], properly arranged nano-apertures [29], possibly combined with circular  
83 diffraction gratings [30,31]. Such results rely on the fact that OAM possessed by surface plasmons  
84 can be further manipulated and transferred to freely propagating radiation [28,32].

85 Here we propose an alternative way of producing vortex beam, by exploiting Bloch Surface Waves  
86 [33,34] on dielectric multilayers as a mean to transfer energy, momentum and OAM to a free-space  
87 propagating beam. Such a two-step process involves a spin-orbit conversion from a focused circularly  
88 polarized beam into radially propagating BSWs and a BSW diffraction in free-space, with an  
89 additional geometric phase imparted by a chiral diffraction grating. Such a BSW-based approach can  
90 benefit from the multilayer low absorption that is potentially suitable for light source integration and  
91 an additional degree of freedom in the polarization state of coupled BSWs, which can be either TE-  
92 or TM-polarized depending on the multilayer design [35].

93 The setup and the sample structure are shown in Figure 1 and described in detail in the Methods  
94 section. Briefly, in Figure 1a, a circularly polarized Gaussian CW laser beam ( $\lambda=532$  nm) is expanded  
95 and spatially filtered by means of a properly sized circular Beam Blocker. An oil-immersion, high  
96 NA objective is back-contacted to a multilayer glass substrate, in order to focus the incoming beam  
97 onto a flat area of the top surface. The multilayer is made of a stack of multiple Ta<sub>2</sub>O<sub>5</sub> and SiO<sub>2</sub> layers,  
98 topped by a 75 nm-thick PMMA film (Figure 1b,c). Thanks to the beam blocker, only focused light  
99 propagating at angles larger than the glass/air critical angle  $\theta_c$  can reach the sample. A fraction of the  
100 incoming power is thus available for coupling to BSWs, provided that wavelength, momentum and  
101 polarization matching conditions are fulfilled, as indicated by the BSW dispersion curve for TE-  
102 polarization [36]. Since the coupling mechanism is polarization-sensitive and the incident electric  
103 field is circularly polarized, BSWs are spreading radially from the focused spot area, with an  
104 accumulated phase delay that is linearly varying with the azimuthal angle of the propagation direction.  
105 As a result, a BSW propagating radially on the multilayer surface is obtained, with a peculiar spiral-  
106 like wavefront profile (see Supporting Information), analogous to plasmonic vortices [26].  
107 Surrounding the flat coupling region, an axis-symmetric diffractive grating is etched in the PMMA  
108 layer. The grating operates as an outcoupler, by diffracting BSWs out-of-plane in both substrate  
109 (glass) and cladding (air) media, along a direction close-to-normal to the sample surface (order of  
110 diffraction  $n=-1$ ) [37]. Depending on the grating shape (e.g. circular or spiral-like), an additional

111 geometrical phase profile can be imparted to the diffracted radiation. In previous applications, this  
 112 feature has been exploited for steering the diffracted beam [38,39]. The outcoupled power is then  
 113 collected by the same high-NA objective and Fourier-transformed before being imaged on the camera  
 114 plane. A linear polarizer and a quarter-wave plate allow for a polarization analysis on the collected  
 115 images. If the beam blocker is removed, an interference pattern as shown in Figure 1 can be obtained.  
 116 In this exemplary case, the spiral-shaped interference fringes result from the superposition of a  
 117 diffracted vortex beam (OAM number  $\ell = 1$ ) and light reflected from the sample surface [32].



118  
 119 **Figure 1.** a) Sketch of the experimental setup. L<sub>1-4</sub> Plano-Convex lenses, LP<sub>1,2</sub> Polarizers, QW<sub>1,2</sub>  
 120 Quarter-wave Plates, BB Beam Blocker, BS Beamsplitter, BFP Back Focal Plane. In the exemplary  
 121 BFP image, an interference pattern is shown, due to the superposition of a diffracted vortex beam and  
 122 a reflected spherical wave from the sample surface. No Beam Blocker has been used in this case. b)  
 123 Detailed view of the BSW coupling and diffraction mechanism. Illumination is provided by means  
 124 of a beam-blocked circularly polarized laser beam focused through an oil immersion objective, such  
 125 that the minimum incidence angle is slightly above the critical angle  $\theta_c$ , in order to match the BSW  
 126 coupling conditions. c) Sketch of the multilayer structure with an exemplary spiral diffraction grating  
 127 fabricated in PMMA on top (not to scale).

## 128 RESULTS AND DISCUSSION

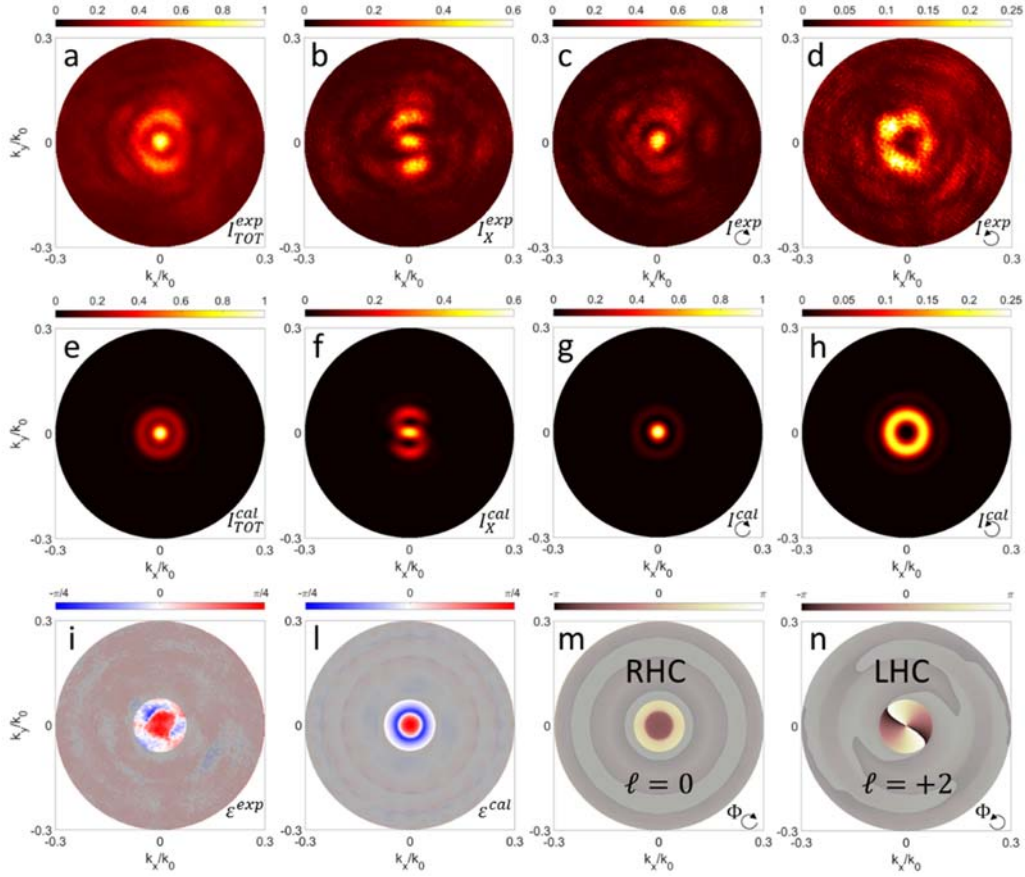
129 In this section, experimental results are presented related to (i) a circular-symmetric annular grating  
130 with topological charge  $m=0$ , (ii) a single-arm spiral grating, (iii) a double-arm spiral grating. In the  
131 last two cases, both handedness of the incident polarization are considered, namely Right-Handed  
132 Circular (RHC) and Left-Handed Circular (LHC) polarizations, such that the incident beam Spin  
133 Angular Momentum (SAM) and the grating topological charge can have either equal or opposite sign.  
134 In order to evaluate the polarization state of the diffracted light, the polarization ellipse  
135 parameter  $\varepsilon(k_x, k_y) = \frac{1}{2} \arg(\sqrt{S_1^2 + S_2^2} + iS_3)$  is calculated across the BFP, where  $S_1$ ,  $S_2$  and  $S_3$  are  
136 the Stokes parameters [40]. Right-Handed Circular (RHC), Left-Handed Circular (LHC) and Linear  
137 Polarizations (LP) correspond to  $\varepsilon_{RHC} = \frac{\pi}{4}$ ,  $\varepsilon_{LHC} = -\frac{\pi}{4}$  and  $\varepsilon_{LP} = 0$  respectively. Polarization-  
138 filtered raw images and Stokes parameter distributions for the structures considered here are shown  
139 in the Supporting Information.

140 A numerical 3D model based on a commercial Finite-Difference Time-Domain (FDTD) solver  
141 (Lumerical Inc.) is used to support the interpretation of the experimental observations. In order to  
142 mimic the focused circularly polarized beam underlying the BSW coupling, a pair of (coherent) linear  
143 orthogonal dipoles laying on the multilayer plane and oscillating with a  $\frac{\pi}{2}$  relative phase delay are  
144 introduced (see Supporting Information Movie S2). Further details on the validity of this model are  
145 provided in the Methods section.

146 **Circular Outcoupler ( $m=0$ ).** In this configuration, a RHC circular polarization ( $\varepsilon = \frac{\pi}{4}$ ) is employed  
147 to couple BSWs that are then diffracted. As shown in Figure 2a,e, the total intensity collected on the  
148 BFP exhibits a maximum at  $k_x=k_y=0$ , corresponding to a constructive interference condition for light  
149 traveling along a direction perpendicular to the multilayer surface. A linear-polarization filtering  
150 reveals the presence of a pair of spiral-like arms spreading from the central maximum that rotate as  
151 the polarization analyser is rotated (in Figure 2b,e the measured and calculated intensity of the x-  
152 component of the diffracted light are presented). Without the polarization filter, the spiral-like arms

153 merge together to form a ring surrounding the central maximum. When polarization-projected onto a  
154 RHC polarization state, the intensity pattern has still a maximum in the BFP center (Figure 2c,g),  
155 while a weak ring is obtained for a projection onto a LHC polarization state (Figure 2d,h). A  
156 comparison between the distributions for the measured and the calculated parameter  $\varepsilon(k_x, k_y)$  on the  
157 BFP indicates that the central maximum is substantially RHC polarized, i.e.  $\varepsilon(0,0) \cong \frac{\pi}{4}$ , while the  
158 outer ring is LHC polarized, i.e.  $\varepsilon(0,0) \cong -\frac{\pi}{4}$  (Figure 2i,l).

159 By enforcing the conservation of the Total Angular Momentum  $J$ , which also takes into account the  
160 topological charge  $m$  imparted by the diffraction grating, the following equation applies:  $\sigma_i + m =$   
161  $1 + 0 = \sigma_o + \ell$ , where  $\sigma_o$  is the output SAM number and  $\ell$  is the corresponding OAM number. The  
162 solution to this equation is not unique. In particular, two SAM-OAM configurations are possible: a  
163 RHC beam preserving the input polarization and carrying zero OAM, i.e.  $\sigma_o = +1$  and  $\ell = 0$ , and a  
164 doughnut LHC beam with a reverse polarization, with  $\sigma_o = -1$  and OAM with  $\ell = +2$ . The two  
165 beams are partially overlapped. This observation is supported by the phase distribution calculated for  
166 the RHC and the LHC polarized fields presented in Figure 2m,n: a flat wavefront with constant phase  
167 is found for the RHC beam ( $\ell = 0$ ) and a spiral wavefront with two  $2\pi$  discontinuities for the LHC  
168 beam ( $\ell = +2$ ).



169

170 **Figure 2.** BFP Diffraction patterns from a circular outcoupler ( $m = 0$ ). Incident polarization is RHC.

171 a,e) experimental and calculated total intensity showing a central spot surrounded by a weak outer

172 ring; b,f) experimental and calculated x-polarized intensity; c,g) experimental and calculated RHC

173 intensity showing a central spot; d,h) experimental and calculated LHC intensity showing a doughnut

174 shape; i,l) experimental and calculated polarization ellipse parameter  $\varepsilon(k_x, k_y)$  with the sign reversal

175 from the inner area to the outer ring; m) calculated phase of the diffracted field with RHC polarization,

176 showing a constant distribution; n) calculated phase of the diffracted field with LHC polarization,

177 showing two  $2\pi$  discontinuities.

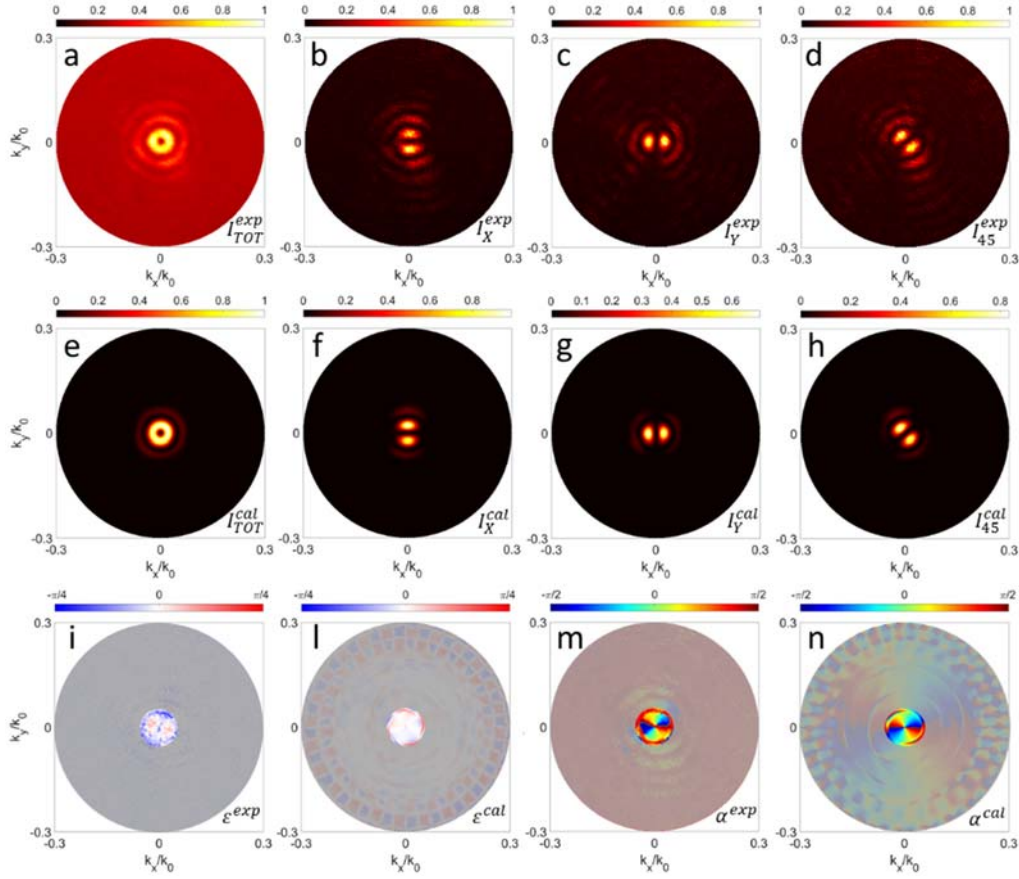
178

179 **Spiral Outcoupler ( $m = -1$ ).** BSWs are first coupled with an input RHC polarization ( $\sigma_i = +1$ )

180 and made interacting by a spiral grating with opposite handedness ( $m = -1$ ). The corresponding

181 intensity pattern is shown in Figure 3a,e.





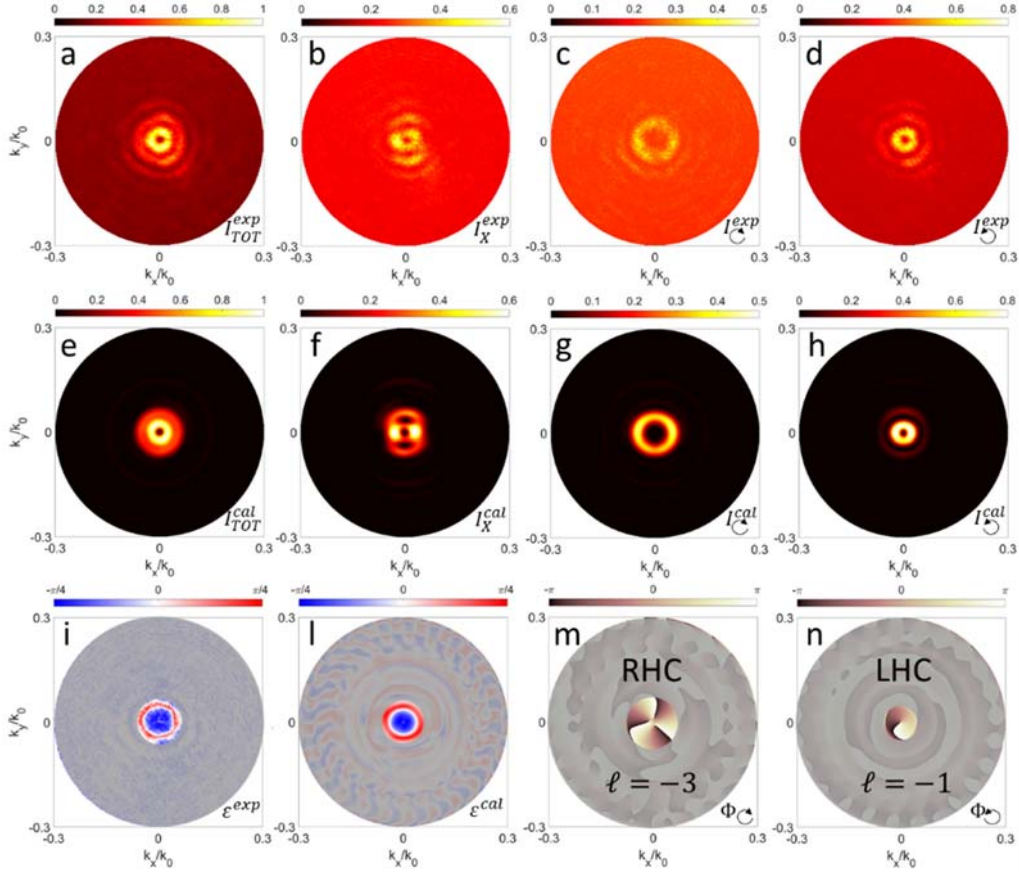
182  
 183 **Figure 3.** BFP Diffraction patterns from a 1-arm spiral outcoupler ( $m = -1$ ). Incident polarization  
 184 is RHC. a,e) experimental and calculated total intensity showing a doughnut shape; b,f) experimental  
 185 and calculated x-polarized intensity; c,g) experimental and calculated y-polarized intensity; d,h)  
 186 experimental and calculated 45°-polarized intensity; i,l) experimental and calculated polarization  
 187 ellipse parameter  $\varepsilon(k_x, k_y)$  indicating a substantially linear polarization state  $\varepsilon \cong 0$ ; m,n)  
 188 experimental and calculated ellipse parameter  $\alpha(k_x, k_y)$  indicating an azimuthal orientation of the  
 189 electric field.

190  
 191 The phase delay profile imparted by the diffractive structure onto the diffracted BSWs results in a  
 192 destructive interference such that a zero-intensity phase singularity is produced at  $k_x=k_y=0$ . When  
 193 filtered with the linear polarizer LP<sub>1</sub> (e.g. oriented along the x, y or 45° direction), two-lobe patterns  
 194 are found, whose orientation is perpendicular to the analyser transmission axis (Figures 3b-d).  
 195 Calculated intensity patterns are in good agreement with the experimental observations (Figures 3f-  
 196 h). The distribution of the parameter  $\varepsilon(k_x, k_y)$  shows a substantially linear polarization corresponding  
 197 to the doughnut ( $\varepsilon \cong 0$ ) (Figures 3i,l). The uniformity of the polarization orientation is evaluated by

198 extracting the parameter  $\alpha(k_x, k_y) = \frac{1}{2} \text{arg}(S_1 + iS_2)$ , which provides the local orientation of the  
 199 polarization ellipse (almost a line, in this case) across the BFP [40]. In Figures 3m,n both the  
 200 experimental and the calculated distributions for  $\alpha(k_x, k_y)$  indicate that the substantially linear  
 201 polarization follows an axis-symmetric distribution such that the electric field is azimuthally oriented  
 202 about the beam axis in  $k_x = k_y = 0$ . In this case, the  $J$  conservation rule reads as  $\sigma_i + m =$   
 203  $1 - 1 = \sigma_o + \ell = 0$ , leading to an output SAM number  $\sigma_o = 0$  and an OAM  $\ell = 0$ , which is  
 204 consistent with the observed azimuthal polarization state of the output beam.

205 When the illumination polarization is switched to LHC ( $\sigma_i = -1$ ) the input SAM and the grating  
 206 topological charge possess the same sign. The overall intensity pattern having a doughnut shape is  
 207 presented in Figure 4a,e. At a closer look, the output results from the superposition of a pair of ring-  
 208 shaped beams, which are non-interfering because of their orthogonal polarizations. A weak outer ring  
 209 (Figure 4c,g) is imaged upon RHC filtering, while an intense inner ring (Figure 4d,h) is obtained  
 210 upon LHC filtering. The experimental and the calculated distributions for  $\varepsilon(k_x, k_y)$  (Figure 4i,l)  
 211 confirm that the polarization state of the two beams is still substantially circular. However, a reversal  
 212 of handedness from LHC to RHC can be found while moving from the inner ring toward the outer.

213 The two partially overlapped beams must satisfy the  $J$  conservation rule, i.e.  $\sigma_i + m =$   
 214  $-1 - 1 = \sigma_o + \ell = -2$ . A first solution to this equation is represented by a LHC polarized beam  
 215 having the same SAM number as the incident radiation  $\sigma_o = -1$  and OAM  $\ell = -1$ . An orthogonal  
 216 solution is a RHC polarized beam having a reversed SAM  $\sigma_o = +1$  and OAM  $\ell = -3$ . The  
 217 topological charge of the diffracted vortex beams can be directly appreciated from the calculated  
 218 phase distributions of the RHC and LHC polarized beams (Figure 4m,n), exhibiting three and one  $2\pi$   
 219 discontinuities respectively, on the BFP.

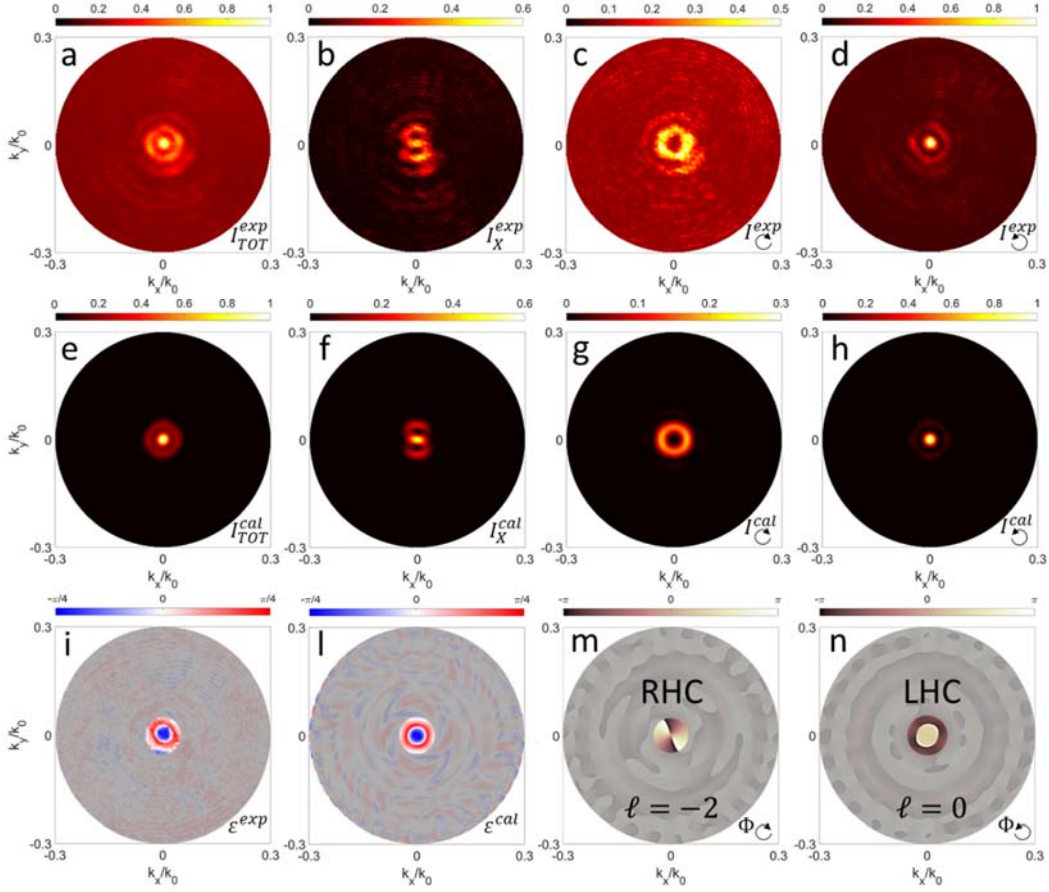


220

221 **Figure 4.** BFP Diffraction patterns from a 1-arm spiral outcoupler ( $m = -1$ ). Incident polarization  
 222 is LHC. a,e) experimental and calculated total intensity showing a superposition of an inner and an  
 223 outer ring-shaped patterns; b,f) experimental and calculated x-polarized intensity; c,g) experimental  
 224 and calculated RHC intensity, distributed according to the outer ring; d,h) experimental and calculated  
 225 LHC intensity; distributed according to the inner ring; i,l) experimental and calculated polarization  
 226 ellipse parameter  $\varepsilon(k_x, k_y)$  indicating a substantially circular polarization with handedness reversal  
 227 from the inner to the outer ring; m) calculated phase of the diffracted field with RHC polarization,  
 228 showing three  $2\pi$  discontinuities; n) calculated phase of the diffracted field with LHC polarization,  
 229 showing one  $2\pi$  discontinuity.

230

231 **Spiral Outcoupler ( $m = -2$ ).** As in the previous configuration, an incident RHC polarization ( $\sigma_i =$   
 232  $+1$ ) is first considered. The overall intensity shown in Figure 5a,e is obtained as the superposition of  
 233 a weak outer ring and a brighter central spot. Both patterns can be individually imaged by operating  
 234 a polarization filtering through a RHC state (Figure 5c,g) and a LHC state (Figure 5d,h), respectively.



235

236

237

238

239

240

241

242

243

244

245

246

247

248

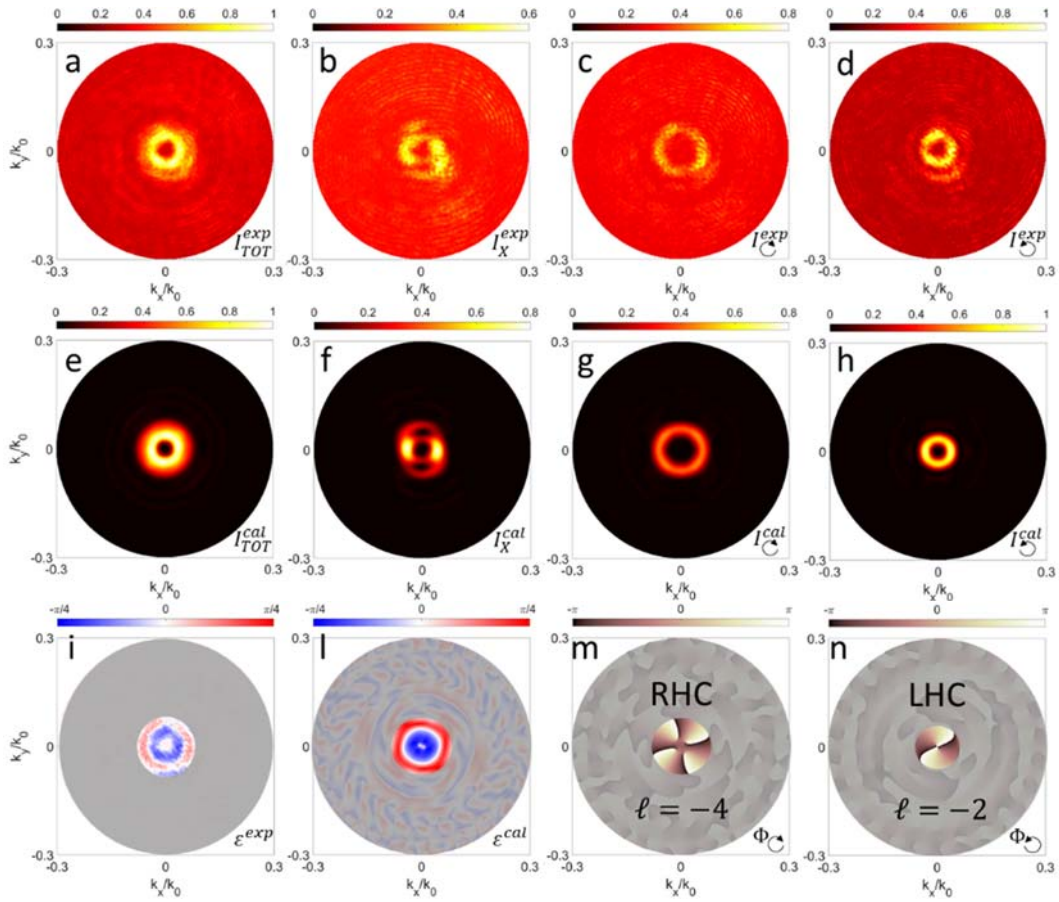
249

250

**Figure 5.** BFP Diffraction patterns from a 2-arms spiral outcoupler ( $m = -2$ ). Incident polarization is RHC. a,e) experimental and calculated total intensity, given by the superposition of a central spot and a weaker outer ring; b,f) experimental and calculated x-polarized intensity; c,g) experimental and calculated RHC intensity, distributed according to the weak outer ring; d,h) experimental and calculated LHC intensity, distributed according to the bright central spot; i,l) experimental and calculated polarization ellipse parameter  $\varepsilon(k_x, k_y)$  indicating a substantially circular polarization, with handedness reversal from the central spot to the outer ring; m) calculated phase of the diffracted field with RHC polarization, showing two  $2\pi$  discontinuities; n) calculated phase of the diffracted field with LHC polarization, showing a uniform phase distribution.

The distribution of the parameter  $\varepsilon(k_x, k_y)$  indicates that the polarization is substantially circular across the pattern. However, the bright central spot shows a LHC polarization state, which is reversed with respect to the incident radiation (Figure 5i). Furthermore, the outer weak ring maintains a LHC polarization, as the illumination (Figure 5l). The conservation of the momentum  $J$  leads to  $\sigma_i + m = +1 - 2 = \sigma_o + \ell = -1$ , which has the following two solutions associated to the observed beams:

251  $\sigma_o = +1$  (RHC) and  $\ell = -2$ ;  $\sigma_o = -1$  (LHC) and  $\ell = 0$ . The calculated phase distributions are  
 252 consistent with the Total Angular Momentum algebra, since the RHC beam has a vortex wavefront  
 253 with two  $2\pi$  discontinuities, while the LHC beam has a flat wavefront (Figure 5m,n). A constant  
 254 phase is also consistent with the existence of a central maximum at  $k_x = k_y = 0$  for the LHC beam.  
 255 For a LHC polarization ( $\sigma_i = -1$ ) a phase singularity is produced on the optical axis, and the overall  
 256 intensity pattern (Figure 6a,e) results from the superposition of a LHC polarized inner ring (Figure  
 257 6c,g) and a RHC polarized outer ring (Figure 6d,h).



258  
 259 **Figure 6.** BFP Diffraction patterns from a 2-arm spiral outcoupler ( $m = -2$ ). Incident polarization  
 260 is LHC. a,e) experimental and calculated total intensity; b,f) experimental and calculated x-polarized  
 261 intensity; c,g) experimental and calculated RHC intensity; d,h) experimental and calculated LHC  
 262 intensity; i,l) experimental and calculated polarization ellipse parameter  $\epsilon(k_x, k_y)$ ; m) calculated  
 263 phase of the diffracted field with RHC polarization showing four  $2\pi$  discontinuities; n) calculated  
 264 phase of the diffracted field with LHC polarization, showing two  $2\pi$  discontinuities.

265



266 Measured and calculated  $\varepsilon(k_x, k_y)$  show the handedness reversal occurring when departing from the  
 267 optical axis toward larger propagation angles, wherein the inner ring preserves the same polarization  
 268 as the incident radiation (Figure 6i,l). From the conservation of the momentum  $J$ , we have:  $\sigma_i + m =$   
 269  $-1 - 2 = \sigma_o + \ell = -3$ , which has the following solutions:  $\sigma_o = +1$  (RHC) and  $\ell = -4$ ;  $\sigma_o = -1$   
 270 (LHC) and  $\ell = -2$ . In this case, both beams exhibit a phase vorticity, with four  $2\pi$  discontinuities  
 271 for the RHC (Figure 6m) state and two  $2\pi$  discontinuities for the LHC state (Figure 6n).

272

## 273 CONCLUSION

274 To conclude, a new mechanism for the generation of vectorial vortex beams has been presented, based  
 275 on spin-orbit interactions involving coupling and diffraction of BSWs. Generally speaking, this kind  
 276 of effects relies on the coherence characteristics of the radiation involved. For this reason, we  
 277 employed a laser beam as an external free-space radiation for coupling BSWs that are subsequently  
 278 diffracted, with an imparted geometrical phase. Several combinations of polarization states and OAM  
 279 are obtained, as summarized in Table 1. Further options for vortex beam generation carrying OAM  
 280 with other polarization configurations can be possibly produced by means of multilayers supporting  
 281 TM-polarized, in addition to TE-polarized BSWs [41].

	<b>Grating Topological Charge <math>m</math></b>	$m = 0$	$m = -1$	$m = -2$
<b>Incident SAM <math>\sigma_i</math></b>				
$\sigma_i = +1$		$\sigma_o = -1 \ \& \ \ell = +2$ $\sigma_o = +1 \ \& \ \ell = 0$	$\sigma_o = 0 \ \& \ \ell = 0$	$\sigma_o = -1 \ \& \ \ell = 0$ $\sigma_o = +1 \ \& \ \ell = -2$
$\sigma_i = -1$		$\sigma_o = -1 \ \& \ \ell = 0$ $\sigma_o = +1 \ \& \ \ell = -2$	$\sigma_o = -1 \ \& \ \ell = -1$ $\sigma_o = +1 \ \& \ \ell = -3$	$\sigma_o = -1 \ \& \ \ell = -2$ $\sigma_o = +1 \ \& \ \ell = -4$

282 **Table 1.** Summary of the SAM-OAM combinations obtained by diffraction of BSWs coupled from  
 283 either RHC or LHC polarized incident light.

284

285 The numerical model developed here suggests that the presented approach is likely to work regardless  
 286 of the coupling mechanism for BSWs. For example, in the perspective of advanced engineered light

287 sources for free-space applications, BSWs can be launched from a single emitter on the multilayer  
288 surface by virtue of near-field interactions (so-called BSW-coupled emission) [42,43]. Then, chiral  
289 diffractive structures can be used as outcouplers surrounding single sources or even planar BSW  
290 cavities (e.g. as described in ref. [44]) hosting light sources within. Provided the coherence  
291 requirements for the BSW-coupled radiation leaking out of the cavity are satisfied, the diffraction  
292 mechanism for free-space vortex generation remains as reported in the text above. While nanocavities  
293 can be chiral themselves, with a handedness-depending LDOS [45], it has been recently shown that  
294 chiral plasmonic structures can foster sources located on their surface to radiate according to a specific  
295 circular polarization handedness [46]. These strategies provide an unprecedented degree of control  
296 on the polarization state of the emitted light. The use of BSWs as a mean for coupling and transferring  
297 energy from sources to free-space, mediated by chiral diffractive gratings, can contribute to enhance  
298 the performance of purely plasmonic nanostructures, which are often limited by the strong absorption  
299 occurring at visible frequencies.

300

## 301 **METHODS**

302 **Experimental setup.** A TEM<sub>00</sub> doubled-frequency Nd:YAG laser beam (GEM, Laser Quantum) is  
303 collimated (L<sub>1</sub>) and transmitted through a first polarization-control box, consisting of a linear  
304 polarizer LP<sub>1</sub> and a quarter wave plate QW<sub>1</sub>. Circular polarization states with both handedness (RH  
305 and LH) are generally produced. A beam blocker is introduced in order to spatially filter the laser  
306 beam, such that an illumination above the glass/air critical angle  $\theta_c$  is provided only. The incoming  
307 beam is focused onto a flat area on the top surface of the multilayer through a  $NA = 1.49$  objective  
308 (Nikon Apo TIRF 1003) that is back-contacted to the glass substrate of the sample. The sample holder  
309 is mounted on a 3-axis piezo stage. When measuring the diffraction patterns from the spiral gratings,  
310 the excitation laser is accurately focused onto the geometric center of the diffraction gratings.  
311 Diffracted light on the glass side is collected by the same objective and directed toward the collection  
312 arm of the setup, after passing through a 50/50 beam splitter. A second polarization-control box

313 consisting of a quarter wave plate  $QW_2$  and a linear polarizer  $LP_2$  filters the outgoing wave onto the  
314 desired polarization state (RHC, LHC or LP). Subsequently, the lens  $L_4$  images the BFP of the  
315 objective onto a CMOS camera (Thorlabs HR-CMOS DCC3260M). With no Beam Blocker, an  
316 interference pattern appears in the BFP image, due to the superposition of the light reflected by the  
317 multilayer inside the light cone ( $NA \leq 1$ ) with the diffracted BSW patterns, eventually carrying  
318 OAM. As a result, spiral-like interference fringes can be observed depending on the OAM number  $\ell$ ,  
319 as shown in Figure S3 [32].

320 **Sample fabrication.** The 1DPC consists of a dielectric multilayer made of a stack of  $Ta_2O_5$  (high  
321 refractive index) and  $SiO_2$  (low refractive index) layers, deposited on a glass coverslip (150  $\mu m$   
322 thickness) by plasma ion-assisted deposition under high vacuum conditions (APS904 coating system,  
323 Leybold Optics). The stack sequence is substrate- $[Ta_2O_5-SiO_2]_x-Ta_2O_5-SiO_2-PMMA$  with 15 layers  
324 in total, including PMMA. The  $Ta_2O_5$  layer (refractive index  $n_{Ta_2O_5}=2.08$ ) is 95 nm thick, the  $SiO_2$   
325 layer (refractive index  $n_{SiO_2}=1.46$ ) is 137 nm thick. The top  $SiO_2$  layer on top of the stack is 127 nm  
326 thick. On top of the structure a 75 nm thick layer of PMMA is spun for pattern fabrication  
327 ( $n_{PMMA}=1.48$ ). Chiral diffractive structures are fabricated by electron beam lithography.

328 **Numerical modeling.** Numerical modeling is performed using the Finite-Difference Time-Domain  
329 method in the Lumerical Inc. software. In order to mimic the focused circularly polarized light  
330 coupling to BSWs, a pair of orthogonal dipolar emitters are positioned at the geometric center of the  
331 spiral grating. More specifically, the emitters are placed 10 nm above the PMMA layer, with the  
332 dipole momentum laying parallel to the multilayer surface, such that the TE polarization of the BSW  
333 can be matched. The two oscillators are phase-shifted by  $\pm \pi/2$ . In this way, thanks to a near-field  
334 interaction, part of the radiated energy from the dipoles is transferred to BSWs (BSW-coupled  
335 emission). As shown in Figure S1 and Supporting Movie S2, resulting BSWs are radially propagating,  
336 with a spiral wavefront due to the time-varying polarization matching conditions of the field given  
337 by the coherent sum of the radiation from the two dipoles.



338 The diffraction gratings are modeled as circular or spiral grooves in the PMMA layers, with a spatial  
339 period  $\Lambda=450$  nm. The total simulation region has dimensions  $(15 \times 15 \times 2.6)$   $\mu\text{m}^3$ . Boundary  
340 conditions are set as perfectly matched layers. The smallest mesh size is 23 nm. The electromagnetic  
341 near-field is collected using a spatial monitor over a plane 20 nm above the PMMA layer. A near-to  
342 far-field projection technique is applied to calculate the field at a distance of 1 m from the structure,  
343 on the air side. A cylindrical Perfect Electric Conductor, placed 50 nm above the dipole sources, have  
344 been introduced in order to avoid the direct free-space emission from the sources, which could  
345 produce interference with the BSW-diffracted radiation we want to investigate. This metallic plate  
346 mimic the role of the Beam Blocker in the experimental setup. With this arrangement, only the air-  
347 side far-field patterns are calculated. However, as the propagation angles of the diffracted beams (with  
348 respect to the multilayer normal) are very small, the refraction effects are negligible and the far-field  
349 patterns are expected to be similar to those on the glass substrate side.

350

## 351 ACKNOWLEDGEMENTS

352 This research has been supported by the project FOCUS from the R egion Bourgogne Franche-Comt e  
353 and by grants R01 GM125976 and R21 GM129561 from the National Institute of Health. Part of this  
354 work has been carried out at Nanofacility INRiM, a laboratory supported by the Compagnia di San  
355 Paolo foundation.

356

## 357 REFERENCES

- 358 (1) Yao, A.M.; Padgett. M.J. Orbital angular momentum: origins, behavior and applications. *Adv.*  
359 *Opt. Photon.* **2011**, 3, 161-204.
- 360 (2) Shen, Y.; Wang, X.; Xie, Z.; Min,C.; Fu, X.; Liu Q.; Gong, M.; Yuan, X. Optical vortices 30  
361 years on: OAM manipulation from topological charge to multiple singularities. *Light: Science*  
362 *& Applications* **2019**, 8, 90.
- 363 (3) Yi, X.; Liu, Y.; Ling, X.; Zhou, X.; Ke, Y.; Luo, H.; Wen, S.; Fan, D. Hybrid-order Poincare  
364 sphere. *Physical Review A* **2015**, 91, 023801.
- 365 (4) Ng, J.; Lin, Z.; Chan, C.T. Theory of Optical Trapping by an Optical Vortex Beam. *Physical*  
366 *Review Letters* **2010**, 104, 103601.

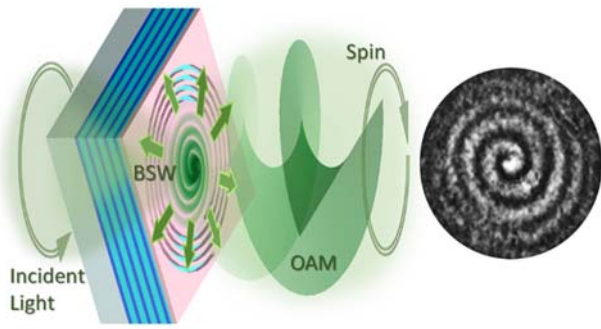
- 367 (5) Cojoc, D.; Garbin, V.; Ferrari, E.; Businaro, L.; Romanato, F.; Di Fabrizio, E. Laser trapping  
368 and micro-manipulation using optical vortices, *Microelectronic Engineering* **2005**, 78–79,125-  
369 131.
- 370 (6) Ma, Y.; Rui, G.; Gu, B.; Cui, Y. Trapping and manipulation of nanoparticles using multifocal  
371 optical vortex metalens. *Scientific Reports* **2017**, 7, 14611.
- 372 (7) Cai, X.; Wang, J.; Strain, M.J.; Johnson-Morris, B.; Zhu, J.; Sorel, M.; O’Brien, J.L.;  
373 Thompson, M.G.; Yu, S. Integrated compact optical vortex beam emitters. *Science* **2012**, 6,  
374 338-363.
- 375 (8) Xie, Z.; Lei, T.; Li, F.; Qiu, H.; Zhang, Z.; Wang, H.; Min, C.; Du, L.; Li, Z.; Yuan, X. Ultra-  
376 broadband on-chip twisted light emitter for optical communications. *Light: Science &*  
377 *Applications* **2018**, 7, 18001
- 378 (9) Wei, S.; Lei, T.; Du, L.; Zhang, C.; Chen, H.; Yang, Y.; Zhu, S.W.; Yuan, X.-C. Sub-100nm  
379 resolution PSIM by utilizing modified optical vortices with fractional topological charges for  
380 precise phase shifting. *Optics Express* **2015**, 23, 30143-30148.
- 381 (10) Chen, L. X.; Lei, J.J.; Romero, J. Quantum digital spiral imaging. *Light: Science & Applications*  
382 **2014**, 3, e153.
- 383 (11) Wang, J.; Yang, J.-Y.; Fazal, I.M.; Ahmed, N.; Yan, Y.; Huang, H.; Ren, Y.; Yue, Y.; Dolinar,  
384 S.; Tur, M.; Willner, A.E. Terabit free-space data transmission employing orbital angular  
385 momentum multiplexing. *Nature Photonics* **2012**, 6, 488–496.
- 386 (12) Ruffato, G.; Massari, M.; Romanato, F. Diffractive optics for combined spatial-and mode-  
387 division demultiplexing of optical vortices: design, fabrication and optical characterization.  
388 *Scientific reports* **2016**, 6, 24760.
- 389 (13) Wang, X.; Nie, Z.; Liang, Y.; Wang, J.; Li, T.; Jia, B. Recent advances on optical vortex  
390 generation. *Nanophotonics* **2018**, 7, 1533-1556.
- 391 (14) Marrucci, L.; Manzo, C.; Paparo, D. Optical Spin-to-Orbital Angular Momentum Conversion  
392 in Inhomogeneous Anisotropic Media. *Physical Review Letters* **2006**, 96, 163905.
- 393 (15) Moreno, I.; Davis, J.; Ruiz, I.; Cottrell, D. Decomposition of radially and azimuthally polarized  
394 beams using a circular-polarization and vortex-sensing diffraction grating. *Optics Express*  
395 **2010**, 18, 7173-7183.
- 396 (16) Cardano, F.; Karimi, E.; Slussarenko, S.; Marrucci, L.; de Lisio, C.; Santamato, E. Polarization  
397 pattern of vector vortex beams generated by q-plates with different topological charges. *Applied*  
398 *Optics* **2012**, 51, C1-C6.
- 399 (17) Genevet, P.; Lin, J.; Kats, M.A.; Capasso, F. Holographic detection of the orbital angular  
400 momentum of light with plasmonic photodiodes. *Nature Communications* **2012**, 3, 1278.

- 401 (18) Lin, J.; Genevet, P.; Kats, M.A.; Antoniou, N.; Capasso, F. Nanostructured holograms for  
402 broadband manipulation of vector beams. *Nano Letters* **2013**, 13, 4269-4274.
- 403 (19) Zhan, A.; Colburn, S.; Trivedi, R.; Fryett, T.K.; Dodson, C.M.; Majumdar, A. Low-Contrast  
404 Dielectric Metasurface Optics. *ACS Photonics* **2016**, 3, 209-214.
- 405 (20) Zhou, Y.; Gao, H.; Teng, J.; Luo, X.; Hong, M. Orbital angular momentum generation via a  
406 spiral phase microsphere. *Optics Letters* **2018**, 43, 34-37.
- 407 (21) Yue, F.; Wen, D.; Xin, J.; Gerardot, B.D.; Li, J.; Chen, X. Vector Vortex Beam Generation with  
408 a Single Plasmonic Metasurface. *ACS Photonics* **2016**, 3, 1558–1563.
- 409 (22) Huang, Y.-W.; Rubin, N.A.; Ambrosio, A.; Shi, Z.; Devlin, R.C.; Qiu, C.-W.; Capasso, F.  
410 Versatile total angular momentum generation using cascaded J-plates. *Optics Express* **2019**, 27,  
411 7469-7484.
- 412 (23) Bouchard, F.; De Leon, I.; Schulz, S.A.; Upham, J.; Karimi, E.; Boyd, R.W. Optical spin-to-  
413 orbital angular momentum conversion in ultra-thin metasurfaces with arbitrary topological  
414 charges. *Applied Physics Letters* **2014**, 105, 101905.
- 415 (24) Maguid, E.; Chriki, R.; Yannai, M.; Kleiner, V.; Hasman, E.; Friesem, A.A.; Davidson, N.  
416 Topologically Controlled Intracavity Laser Modes Based on Pancharatnam-Berry Phase. *ACS*  
417 *Photonics* **2018**, 551817-1821
- 418 (25) Wang, Z.; Wang, Y.; Adamo, G.; Teng, J.; Sun, H. Induced Optical Chirality and Circularly  
419 Polarized Emission from Achiral CdSe/ZnS Quantum Dots via Resonantly Coupling with  
420 Plasmonic Chiral Metasurfaces. *Laser & Photonics Reviews* **2019**, 13, 1800276.
- 421 (26) Kim, H.; Park, J.; Cho, S.-W.; Lee, S.-Y.; Kang, M.; Lee, B. Synthesis and Dynamic Switching  
422 of Surface Plasmon Vortices with Plasmonic Vortex Lens. *Nano Letters* **2010**, 10, 529-536.
- 423 (27) Rui, G.; Nelson, R.L.; Zhan, Q. Beaming photons with spin and orbital angular momentum via  
424 a dipole-coupled plasmonic spiral antenna," *Optics Express* **2012**, 18819-18826.
- 425 (28) Yu, H.; Zhang, H.; Wang, Y.; Han, S.; Yang, H.; Xu, X.; Wang, Z.; Petrov, V.; Wang, J.  
426 Optical orbital angular momentum conservation during the transfer process from plasmonic  
427 vortex lens to light. *Scientific Reports* **2013**, 3, 3191.
- 428 (29) Jiang, Q.; Pham, A.; Berthel, M; Huant, S.; Bellessa, J.; Genet, C.; Drezet, A. Directional and  
429 Singular Surface Plasmon Generation in Chiral and Achiral Nanostructures Demonstrated by  
430 Leakage Radiation Microscopy. *ACS Photonics* **2016**, 3, 1116-1124.
- 431 (30) Gorodetski, Y.; Shitrit, N.; Bretner, I.; Kleiner, V.; Hasman, E. Observation of Optical Spin  
432 Symmetry Breaking in Nanoapertures. *Nano Letters* **2009**, 9, 3016-3019.
- 433 (31) Zhang, B.; Hu, C.; Tang, B.; Hao, J.; Zhang, X.; Sun, M.; Ding, J. Chiral plasmonic lens with  
434 Archimedes-spiral distributed nanoslits. *Journal of Nanophotonics* **2019**, 13, 026008.

- 435 (32) Gorodetski, Y.; Drezet, A.; Genet, C.; Ebbesen, T.W. Generating Far-Field Orbital Angular  
436 Momenta from Near-Field Optical Chirality. *Physical Review Letters* **2013**, 110, 203906.
- 437 (33) Robertson, W.M.; May, M.S. Surface electromagnetic wave excitation on one-dimensional  
438 photonic band-gap arrays. *Applied Physics Letters* **1999**, 74, 1800.
- 439 (34) Liscidini, M.; Galli, M.; Patrini, M.; Loo, R.W.; Goh, M.C.; Ricciardi, C.; Giorgis, F.; Sipe, J.  
440 E. Demonstration of diffraction enhancement via Bloch surface waves in a-SiN:H multilayers.  
441 *Applied Physics Letters* **2009**, 94, 043117.
- 442 (35) Sinibaldi, A.; Fieramosca, A.; Rizzo, R.; Anopchenko, A.; Danz, N.; Munzert, P.; Magistris,  
443 C.; Barolo, C.; Michelotti, F. Combining label-free and fluorescence operation of Bloch surface  
444 wave optical sensors. *Optics Letters* **2014**, 39, 2947-2950.
- 445 (36) Angelini, A.; Barakat, E.; Munzert, P.; Boarino, L.; De Leo, N.; Enrico, E.; Giorgis, F.; Herzig,  
446 H.P.; Pirri, C.F.; Descrovi, E. Focusing and extraction of light mediated by Bloch surface  
447 waves. *Scientific Reports* **2014**, 4, 5428.
- 448 (37) Angelini, A.; Enrico, E.; de Leo, N.; Munzert, P.; Boarino, L.; Michelotti, F.; Giorgis, F.;  
449 Descrovi, E. Fluorescence diffraction assisted by Bloch surface waves on a one-dimensional  
450 photonic crystal. *New Journal of Physics* **2013**, 15, 073002
- 451 (38) Rui, G.; Abeysinghe, D.C.; Nelson, R.L.; Zhan, Q. Demonstration of beam steering via dipole-  
452 coupled plasmonic spiral antenna. *Scientific Reports* **2013**, 3, 2237.
- 453 (39) Angelini, A.; Munzert, P.; Enrico, E.; De Leo, N.; Scaltrito, L.; Boarino, L.; Giorgis, F.;  
454 Descrovi, E. Surface-Wave-Assisted Beaming of Light Radiation from Localized Sources. *ACS*  
455 *Photonics* **2014**, 1, 612–617.
- 456 (40) Röhrich, R.; Hoekmeijer, C.; Osorio, C.I.; Koenderink, A.F. Quantifying single plasmonic  
457 nanostructure far-fields with interferometric and polarimetric k-space microscopy. *Light-*  
458 *Science & Applications* **2018**, 7, 65.
- 459 (41) Pellegrini, G.; Finazzi, M.; Celebrano, M.; Duò, L.; Biagioni, P. Chiral surface waves for  
460 enhanced circular dichroism. *Physical Review B* **2017**, 95, 241402.
- 461 (42) Liscidini, M.; Galli, M.; Shi, M.; Dacarro, G.; Patrini, M.; Bajoni, D.; Sipe, J.E. Strong  
462 modification of light emission from a dye monolayer via Bloch surface waves. *Optics Letters*  
463 **2009**, 34, 2318-2320.
- 464 (43) Badugu, R.; Mao, A.; Blair, S.; Zhang, D.; Descrovi, E.; Angelini, A.; Huo, Y.; Lakowicz, J.R.  
465 Bloch Surface Wave-Coupled Emission at Ultra-Violet Wavelengths. *Journal of Physical*  
466 *Chemistry C* **2016**, 120, 28727-28734.

- 467 (44) Stella, U.; Boarino, L.; de Leo, N.; Munzert, P.; Descrovi, E. Enhanced directional light  
468 emission assisted by resonant Bloch Surface Waves in circular cavities. *ACS Photonics* **2019**,  
469 6, 2073-2082.
- 470 (45) Pham, A.; Berthel, M.; Jiang, Q.; Bellessa, J.; Huan, S.; Genet, C.; Drezet, A. Chiral optical  
471 local density of states in a spiral plasmonic cavity. *Physical Review A* **2016**, 94, 053850.
- 472 (46) Pachidis, P.; Cote, B.M.; Ferry, V.E. Tuning the polarization and directionality of  
473 photoluminescence of achiral quantum dot films with chiral nanorod dimer arrays: implications  
474 for luminescent applications. *ACS Applied Nano Materials* **2019**, 2, 5681-5687.

475 **GRAPHICAL TOC ENTRY**



476